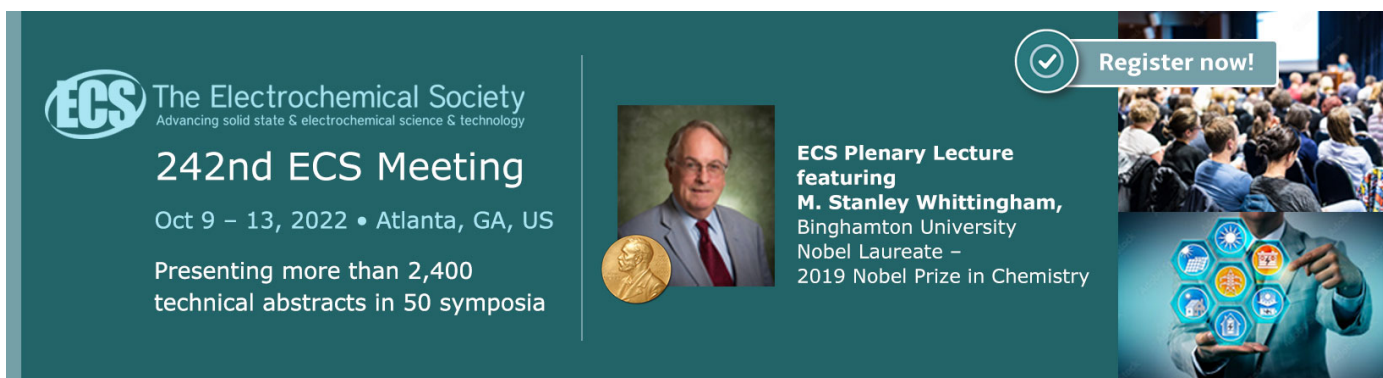


OPEN ACCESS

Preparation of Mesoporous/Microporous MnCo_2O_4 and Nanocubic MnCr_2O_4 Using a Single Step Solution Combustion Synthesis for Bifunction Oxygen Electrocatalysis

To cite this article: Anchu Ashok *et al* 2020 *J. Electrochem. Soc.* **167** 054507

View the [article online](#) for updates and enhancements.

 The Electrochemical Society
Advancing solid state & electrochemical science & technology

242nd ECS Meeting

Oct 9 – 13, 2022 • Atlanta, GA, US


Presenting more than 2,400
technical abstracts in 50 symposia



ECS Plenary Lecture
featuring
M. Stanley Whittingham,
Binghamton University
Nobel Laureate –
2019 Nobel Prize in Chemistry



Register now!





Preparation of Mesoporous/Microporous MnCo_2O_4 and Nanocubic MnCr_2O_4 Using a Single Step Solution Combustion Synthesis for Bifunction Oxygen Electrocatalysis

Anchu Ashok,¹ Anand Kumar,^{1,z} Janarthanan Ponraj,² and Said A. Mansour²

¹Department of Chemical Engineering, College of Engineering, Qatar University, Doha, Qatar

²Qatar Environment and Energy Research Institute (QEERI), Hamad Bin Khalifa University, Qatar Foundation, Doha, Qatar

We report the synthesis of mesoporous/microporous MnCo_2O_4 and cubic MnCr_2O_4 using solution combustion synthesis for oxygen reduction and oxygen evolution reactions. XRD and TEM analysis indicate small crystallites of MnCo_2O_4 forming ultra-thin layer of irregular structures that lead to porous morphology. A slightly larger crystallite size was observed for MnCr_2O_4 . The surface oxygen defect in MnCo_2O_4 is much higher than MnCr_2O_4 that enhances the active sites for the oxygen adsorption and promotes fast dissociation in presence of more exposed Mn/Co sites during the oxygen electrocatalysis. The electrochemical properties of the synthesized catalysts were analysed using CV, LSV, EIS and CA showing high limiting current density and kinetic current density, positive onset and halfwave potential and higher number of overall electron transfer in MnCo_2O_4 than MnCr_2O_4 . Chronoamperometric (CA) runs for 24 h shows excellent stability of MnCo_2O_4 without any significant decrease in the current or potential value in ORR and OER. On basis of the activity and stability performance, MnCo_2O_4 shows to be a promising bifunctional electrocatalyst, with significantly improved performance than previously reported Mn and Co mixed oxides, and comparable to Pt and Ru based catalysts in terms of durability, onset potential and Tafel slope.

© 2020 The Author(s). Published on behalf of The Electrochemical Society by IOP Publishing Limited. This is an open access article distributed under the terms of the Creative Commons Attribution 4.0 License (CC BY, <http://creativecommons.org/licenses/by/4.0/>), which permits unrestricted reuse of the work in any medium, provided the original work is properly cited. [DOI: 10.1149/1945-7111/ab679d]



Manuscript submitted October 3, 2019; revised manuscript received December 6, 2019. Published January 15, 2020. *This paper is part of the JES Focus Issue on Heterogeneous Functional Materials for Energy Conversion and Storage.*

Demand for our energy increases everyday along with the depletion of fossil fuels and environmental issues generated by excessive use of fossil fuels. Researchers around the world are actively pursuing alternative ways of energy generation from renewable and sustainable resources such as batteries, capacitors and fuel cells.^{1,2} Rechargeable metal–air batteries and regenerative fuel cells relying on oxygen electrocatalysis with high theoretical specific energy, energy density, fast charge-discharge mechanism, non-toxic nature and environment friendliness are the ideal choices.^{3,4} These devices require oxygen bifunctional electrocatalysts are high-performance, and capable for both oxygen reduction and evolution reactions (ORR and OER).^{5–8} The main bottle neck of the modern energy storage and conversion devices are the lack of efficient and durable bifunctional oxygen electrocatalyst in the cathode compartment. Platinum (Pt) based electrocatalysts are considered as the most efficient catalysts for oxygen reduction reaction (ORR).^{9–12} Iridium oxide and Ruthenium based catalyst are more promising one towards oxygen evolution reaction (OER).^{13,14} However, a large-scale production and industrial application of these catalysts are slowed down owing to the high cost, limited availability and poor durability of these noble metals.¹⁵

Various non-precious transition metal oxides such as MnO_2 , Co_3O_4 , CeO_2 , NiCo_2O_4 , CuCo_2O_4 , NiFe_2O_4 , ZnMn_2O_4 have been widely studied owing to their electrical conductivity, electrochemical activity, low cost, and its outstanding redox stability in aqueous alkaline solutions.^{16–23} Moreover, the electrochemical properties can be fine-tuned due to the variable valance state and structural flexibility in mixed oxide catalysts. Particularly, cobalt based oxides with spinel AB_2O_4 binary oxide structure including NiCo_2O_4 and MnCo_2O_4 exhibits excellent properties as bifunctional OER/ORR catalysts.^{24–26} MnCo_2O_4 is the most commonly used spinel oxide of cobalt–manganese, where Mn and Co reside on the tetrahedral and octahedral sites of the cubic lattice. Manganese oxides (Mn) are the first transition metal oxide that show outstanding performance towards ORR and, to some extent, towards OER.^{27–29} In addition, Co-based oxides are also reported to exhibit excellent properties for both ORR and OER.^{30,31} A

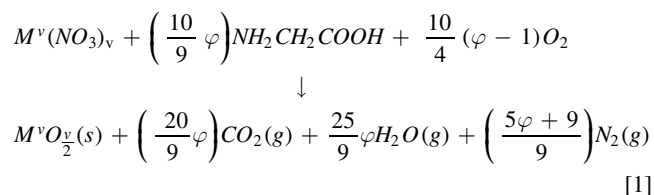
combining both, Mn and Co mixed oxides are expected to synergistically improved the ORR/OER performance further for energy storage and conversion devices. Moreover, Cr_2O_3 have been reported as a promising electrocatalyst because of their high theoretical capacity, low potential and low cost. The ferromagnetic spinel MnCr_2O_4 structure has been widely studied owing to its magnetic and electrical properties. MnCr_2O_4 exhibits much higher resistance towards the carbonaceous attack in many petrochemical industrial processes. MnCr_2O_4 has been used in NO_2 sensing property for YSZ-based potentiometric sensors and growing interest focussed on the synthesis and application of MnCr_2O_4 . To the best of our knowledge, MnCr_2O_4 has not been reported as a bifunctional catalyst onwards ORR/OER activity. Thus, we selected MnCo_2O_4 and MnCr_2O_4 synthesized using solution combustion reaction for the electrochemical reaction.

Li et al. prepared Co_3O_4 modified Mn_3O_4 using citrate method for Zinc–air battery with good cycling ability and outstanding ORR/OER performance.³² Taeseob and co-workers developed MnCo_2O_4 nanoparticles supported on sulphur and nitrogen co-doped mesoporous carbon spheres prepared by the pyrolysis of thiourea and hydrothermal treatment.³³ The as-synthesized catalyst shows excellent performance for ORR/OER and are comparable to that of commercial platinum and ruthenium-based catalyst in terms of durability, onset potential and Tafel slope.³³ Xiaoming, et al. reported the synthesis of dual-phase spinel MnCo_2O_4 (*dp*- MnCo_2O_4) nanocrystals integrated with nanocarbon materials such as nitrogen doped reduced graphene oxide (n-rGO) and carbon nanotubes (CNT) hybrid catalyst with excellent ORR and superior OER activity when compared to 30% platinum supported carbon black (30%Pt/C).³⁴ Chun et al. reported a general synthesis of ultra-small cobalt manganese spinel with controllable phase and composition that catalyses the ORR and OER, exhibiting comparable activity and superior durability to Pt/C.³⁵

Herein, we incorporate solution combustion synthesis (SCS) to prepare a mixed oxide catalysts consisting of Mn, Co and Mn, Cr. SCS is reported to be a single step, fast synthesis process for preparing nanomaterial, particularly oxides/mixed-oxides, with high surface area, high porosity and structural uniformity.^{36–43} Typically, a metal nitrate and glycine (fuel) act as an oxidizer (metal precursor) and reducer, respectively, during the synthesis. The synthesis

^zE-mail: akumar@qu.edu.qa

reaction is believed to be as following:



Where ϕ be the fuel to oxidizer ratio and $\phi > 1$, $\phi < 1$ and $\phi = 1$ are fuel rich, fuel lean and stoichiometric conditions respectively. Based on the amount of fuel used, the properties such as morphology, crystalline nature, composition, oxidation state etc can be easily tuned.³⁶⁻⁴³ We synthesized $MnCr_2O_4$ and $MnCo_2O_4$ using SCS technique and evaluated their electrochemical properties as fuel cells and battery applications.

Experimental

Synthesis of MnM_2O_4 ($M = Co, Cr$).— $MnCo_2O_4$ nanoparticles were synthesized using single step solution combustion synthesis. A 1.2 g of Manganese (II) nitrate tetrahydrate ($Mn(NO_3)_3 \cdot 4H_2O$), a 2.6 g cobalt (II) nitrate hexahydrate ($Co(NO_3)_2 \cdot 6H_2O$) and a 0.742 g of glycine ($C_2H_5NO_2$) were measured based on the stoichiometric equation as reported before.^{30,44-49} The fuel to metal oxidizer ratio was kept at 0.5 to synthesize 1.5 g of nanoparticle. The measured precursors were dissolved in deionized water (DI water) and stirred for approx. 15 min. to get a homogenous solution that was heated over a hot plate at 300 °C until the water evaporated. Once it reaches the ignition temperature, combustion starts at one point of the redox mixture and propagate to the entire beaker. The obtained nanoparticles were crushed using hand motor and sieved it using 75 μm micro sieve to get uniform size nanoparticles. $MnCr_2O_3$ was synthesized by a 1.12 g Manganese (II) nitrate tetrahydrate ($Mn(NO_3)_3 \cdot 4H_2O$), a 3.2 g of chromium (III) nonahydrate ($Cr(NO_3)_3 \cdot 9H_2O$) and 0.927 g of glycine ($C_2H_5NO_2$) in the above procedure.

The catalysts synthesized using SCS was mixed with Vulcan carbon black in order to ensure proper conductivity for electrochemical performance. A 30 mg of the catalyst was mixed with 3.5 ml water and sonicate for 30 min to get a well dispersed particles. Then a 70 mg of carbon black was added slowly while continuing the sonication for another 30 min. Thereafter, the resulted ink was kept over a hot plate heater at 110 °C for drying in order to obtain catalysts/carbon particles.

Material characterization.—The crystalline structure of the products was analyzed using X-ray powder diffractometer (XRD, PANalytical model X'PERT-PRO) with $CuK\alpha$ radiation of wavelength 1.5418 Å, within the range of 10 to 80 degree. The surface morphology were examined using Scanning Electron Microscope (SEM, Nova Nano 450, FEI) and High-Resolution Transmission Electron Microscope (HRTEM, TECNAI G² F20, FEI). Elemental phase mapping of the catalysts were conducted using an EDS (FEI SuperX EDS system) coupled with the TEM. The nanoparticles were dispersed into ethanol and sonicated to get a dispersed solution, which was carefully dropped onto a carbon coated nickel grid (200 mesh), and dried at room temperature to prepare the TEM grids for analysis. The surface elemental composition and the valance state of the synthesized samples were identified using X-ray Photoelectron Spectroscopy (XPS Kratos, AXIS Ultra DLD). AimSizer (AS-3012) was used to identify the BET surface area and pore size analysis of the as-synthesized particles.

Electrochemical measurements.—Electrochemical measurements were carried out on a PINE instrument biopotentiostat (Wave Driver 20) with a three-cell electrode system at room temperature using 1 M KOH electrolyte. A 5 mm diameter glassy

carbon disc mounted over a Teflon RDE housing (PINE instruments) connected to a rotator, with maximum speed of 3600 rpm, was used as a working electrode. A single junction Ag/AgCl (4 M KCl solution) and a Pt coil were used as a reference and counter electrodes respectively. To prepare the working electrode, a 5 mg of catalyst supported on carbon, 300 μl of iso-propyl alcohol and a 30 μl of Nafion binder were mixed together and sonicated for 30 min to obtain a homogenous suspension. A 5 μl of the ink thus formed was dropped onto the working electrode and dried overnight at room temperature. The potential represented in the entire work is with respect to the Ag/AgCl reference electrode. The electrochemical performance was assessed using cyclic voltammetry (CV), linear sweep voltammetry (LSV), chronoamperometry (CA) and electrochemical impedance spectroscopy (EIS). Before conducting the experiments, the 1 M KOH electrolyte was purged with N_2 for 30 min to remove the residual oxygen and unwanted contaminants. During CV, the loaded catalyst was pretreated between a potential window of -0.9 to $+0.9$ V at 500 mVs^{-1} for 100 cycle. The performance of the oxygen electrocatalysts were measured by saturating the electrolyte with highly pure O_2 for 1 hr. The CV was collected in the potential range of 0.4 to -0.9 V at a scan rate of 50 mVs^{-1} . During the LSV, the working electrode was scanned between 0.9 to -0.9 V at a scan rate of 5 mVs^{-1} at different rotor speeds to examine the oxygen reduction reaction and oxygen evolution reaction. The slope of Koutechy-Levich (K-L) plot is calculated to find the overall electron transfer in the reaction using the below equations:

$$\frac{1}{J} = \frac{1}{J_L} + \frac{1}{J_K} = \frac{1}{B\omega^{1/2}} + \frac{1}{J_K} \quad [2]$$

$$B = 0.62nFC_0(D_0)^{2/3}v^{-1/6} \quad [3]$$

$$J_k = nFkC_0 \quad [4]$$

Where J , J_K and J_L are the measured current density, kinetic current density and limiting current density respectively. In addition, ω is the electrode angular rotation velocity, n is the overall electron transfer and k represents the electron-transfer rate constant. The values of Faraday constant, $F = 96485$ C mol^{-1} , the bulk concentration of dissolved O_2 in the electrolyte, $C_0 = 7.8 \times 10^{-7}$ mol cm^{-3} for 1 M KOH, the kinematic viscosity of electrolyte $\nu = 0.01$ $cm^2 s^{-1}$, and the diffusion coefficient $D_0 = 1.9 \times 10^{-5}$ $cm^2 s^{-1}$ were used during the calculations.

Rotating ring disk electrode (RRDE) system used with the same electrochemical workstation under a four-electrode configuration mode, where 5 mm glassy carbon working electrode is in the center and surrounded by a platinum ring with 7.50 mm and 6.5 mm of outer diameter and inner diameter respectively. The collection efficiency (N) of the Pt ring electrode is 25% and the ring potential was held to be constant at $+0.5$ V. The number of electron transfer (n) and H_2O_2 yield (H_2O_2 -%) per oxygen molecule can be calculated using the following equation:

$$n = \frac{4 \times I_D}{I_D + I_R / N} \quad [5]$$

$$H_2O_2 \% = \frac{200 \times I_R / N}{I_D + I_R / N} \quad [6]$$

Where I_D , I_R and N be the disc current, ring current and collection efficiency respectively.

Electrochemical impedance spectroscopy (EIS) of the catalysts at different potential were analyzed using a Zahner Elektrik IM6 electrochemical workstation within a frequency range of 100 kHz to 0.01 Hz under an open circuit potential by applying an AC perturbation voltage of 5 mV amplitude. The potential represented in the work is with respect to Reversible Hydrogen Electrode (RHE) using the equation:

$$E_{\text{(RHE)}} = E_{\text{Ag/AgCl}} + 0.059 \text{ pH} + E^{\circ}_{\text{Ag/AgCl}}$$

Where $E^{\circ}_{\text{Ag/AgCl}} = 0.1976 \text{ V}$ at 25°C and $E_{\text{Ag/AgCl}}$ is your working potential.

Results and Discussion

The crystal structure of the MnCo_2O_4 and MnCr_2O_4 was observed using X-ray diffraction (XRD) as shown in Fig. 1. The diffraction peaks in MnCo_2O_4 at 18.5° , 30.54° , 35.8° , 37.64° , 43.76° , 54.34° , 57.91° and 63.2° could be attributed to the crystal planes (111), (220), (311), (222), (400), (422), (511) and (440) and confirm the formation of well crystallized and pure MnCo_2O_4 with cubic spinel structure (JCPDS No. 23–1237). The structure is in mixed valence oxide form (+2 and +3 oxidation state) where the manganese and cobalt is distributed over tetrahedral (Mn^{2+} and Co^{2+}) and octahedral sites (Mn^{3+} and Co^{3+}).⁵⁰ For MnCr_2O_4 , there exist similar diffraction peaks and crystal planes indexed with a spinel cubic structure along with some weak characteristic peaks of Cr_2O_3 . Figure 1b shows a typical spinel cubic crystal structure of MnCo_2O_4 and MnCr_2O_4 . The crystalline size of the particle calculated from the (311) peak using Scherrer's formula for MnCo_2O_4 and MnCr_2O_4 is found to be 13 nm and 18 nm respectively.⁵¹

Figures 1c–1d shows the SEM image of the as-prepared MnCr_2O_4 and MnCo_2O_4 . Both the microstructure shows the presence of flake like morphology with large micropores. The micropores are formed on the surface due to the evolution of gases during the combustion reaction (Eq. 1). These micropores provide more sites for the adsorption of reactant molecules and thereby enhance electrocatalytic properties. The elemental composition of MnCr_2O_4 and MnCo_2O_4 shows the presence Mn (in MnCo_2O_4 –9.39% and MnCr_2O_4 –8.60%), Co(19.9%)/Cr(15.75) and O (in MnCo_2O_4 –43.69% and MnCr_2O_4 –43.17%) with an approximate molar ratio of Mn/Co (or Cr)/O close to 1:2:4, by offering a stoichiometric formula of MnCo_2O_4 or MnCr_2O_4 . The elemental composition shows that the atomic percentage of carbon is less in Mn–Co oxide (26.95%) when compared to Mn–Cr oxide (32.48%). From our previous studies the existence of carbon in the catalyst masks the active sites and adversely affect the electrocatalytic performance.³⁰

Figure 2 shows the detailed analysis of MnCo_2O_4 using TEM and HRTEM technique. The low magnified image in Fig. 2a shows the formation of particles with ultra-thin layer of irregular transparent structures that are interweaved to form a porous morphology. The interconnected structure is overlaid as a single continuous solid structure with an average size of 500 nm. HRTEM in Fig. 2b shows

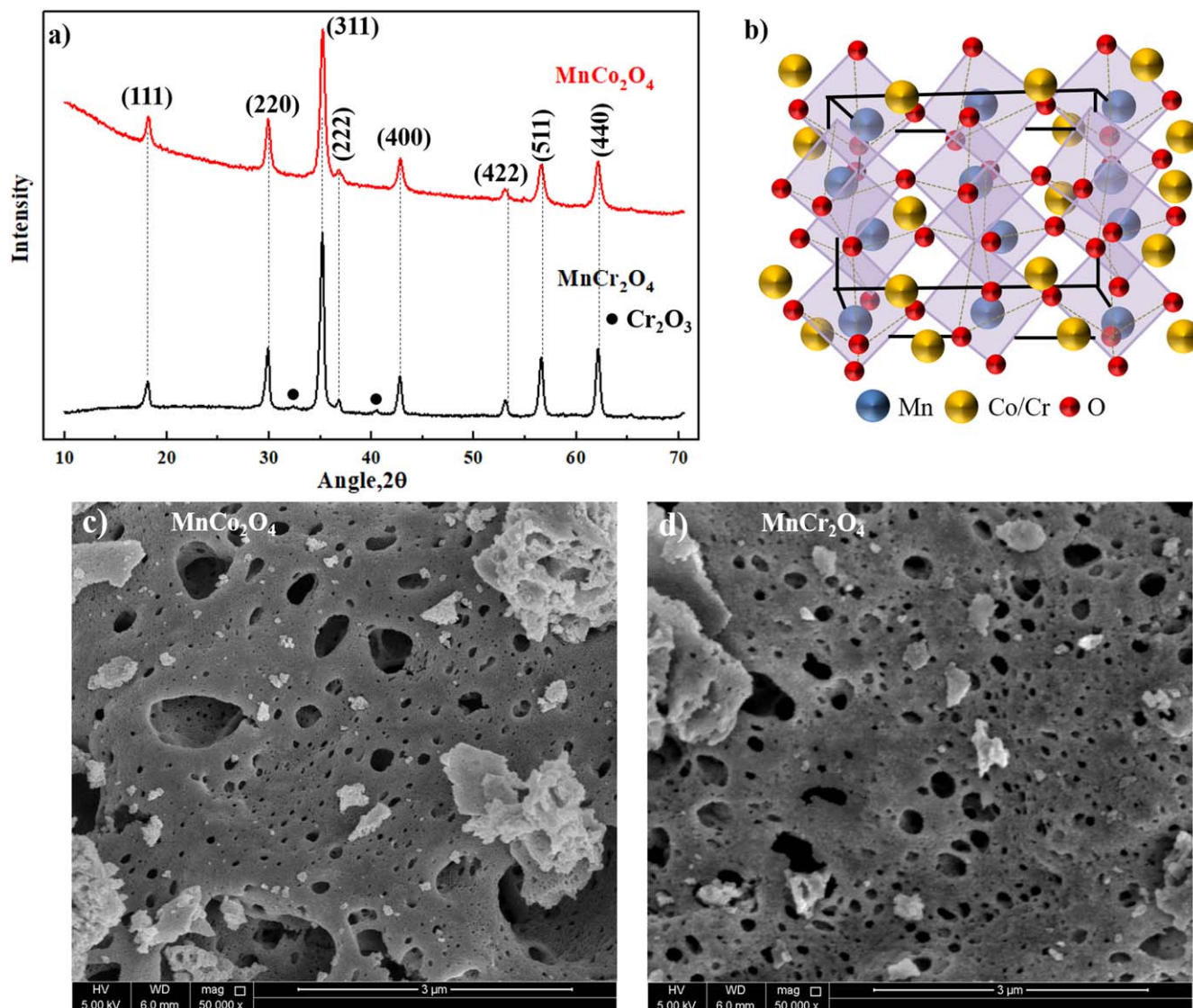


Figure 1. (a) XRD pattern of MnCr_2O_4 and MnCo_2O_4 synthesized using single step solution combustion synthesis (b) typical spinel cubic crystal structure. SEM micrograph of (c) MnCo_2O_4 (d) MnCr_2O_4 .

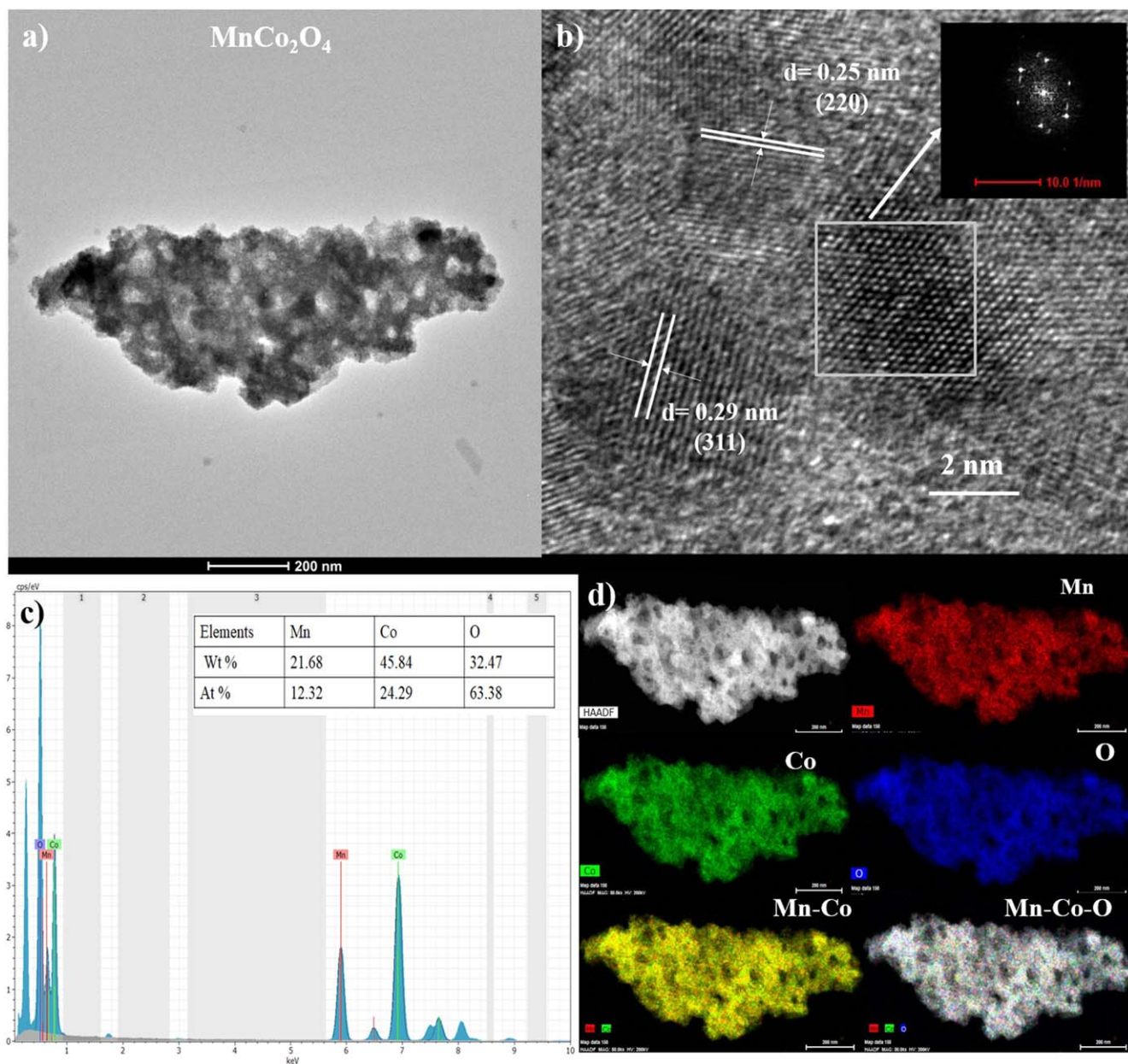


Figure 2. (a) TEM images (b) HRTEM representation (c) EDS spectrum with the elemental composition in inset and (d) elemental phase mapping of individual and combined elements of Mn, Co and O in MnCo_2O_4 as-synthesized using solution combustion technique.

that these solid semi-transparent structures consist of a large number of small crystalline particles of MnCo_2O_4 with average size in the range of 5 nm. The lattice fringes with lattice spacing (d) of about 0.25 nm and 0.29 nm corresponds to the (220) and (311) crystal planes of MnCo_2O_4 , respectively. The presence crystal planes analysed from HRTEM is consistent with the XRD analysis in Fig. 1. The synthesized MnCo_2O_4 exhibits a highly crystalline structure as confirmed with the distinct diffraction dots spotted in the FFT pattern in Fig. 2b (inset). The EDX spectrum and the elemental phase mapping obtained from the high-angle annular dark-field scanning transmission electron microscopy (HAADF-STEM) for the synthesized catalysts is shown in Figs. 2c–2d. The EDX spectrum in Fig. 2c shows that these nanoflakes like structure consist of Mn, Co and O and the molar ratio of Co/Mn is calculated to be 2, which is in well consistent with the SEM-EDX analysis discussed before. The elemental phase mapping further confirms a homogeneous distribution of Mn, Co and O throughout the catalyst surface. The particle morphology of the MnCr_2O_4 can be identified using the TEM

images shown in Fig. 3. The particles obtained appear to be in the form of cubic structure with an average particle size in the range of 30–50 nm. These sharp-edged particles are interconnected as nano-building blocks up to 500 nm as shown in Fig. 3a. The individual particles are linked together with an overlapping of the lattice fringes as shown in Fig. 3a-inset. The lattice fringes with d spacing of 0.21 nm and 0.249 nm corresponds to the (400) and (220) planes of MnCr_2O_4 (Fig. 3b). The clear lattice fringes with FFT pattern confirm the existence of single-crystalline nature of MnCr_2O_4 nanoparticles. HAADF-STEM and elemental mapping in Fig. 3c reveals the uniform distribution of Mn, Cr and O in MnCr_2O_4 nanoparticle.

The oxidation state and the surface chemical composition of the synthesized MnCo_2O_4 and MnCr_2O_4 nanoparticle were identified using X-ray photoelectron spectroscopy (XPS) measurements. Detailed XPS analysis of MnCo_2O_4 and MnCr_2O_4 is shown in Fig. 4. The Mn 2p high-resolution spectrum in Figs. 4a and 4d for MnCo_2O_4 and MnCr_2O_4 consist of two main peaks at 641.9 eV

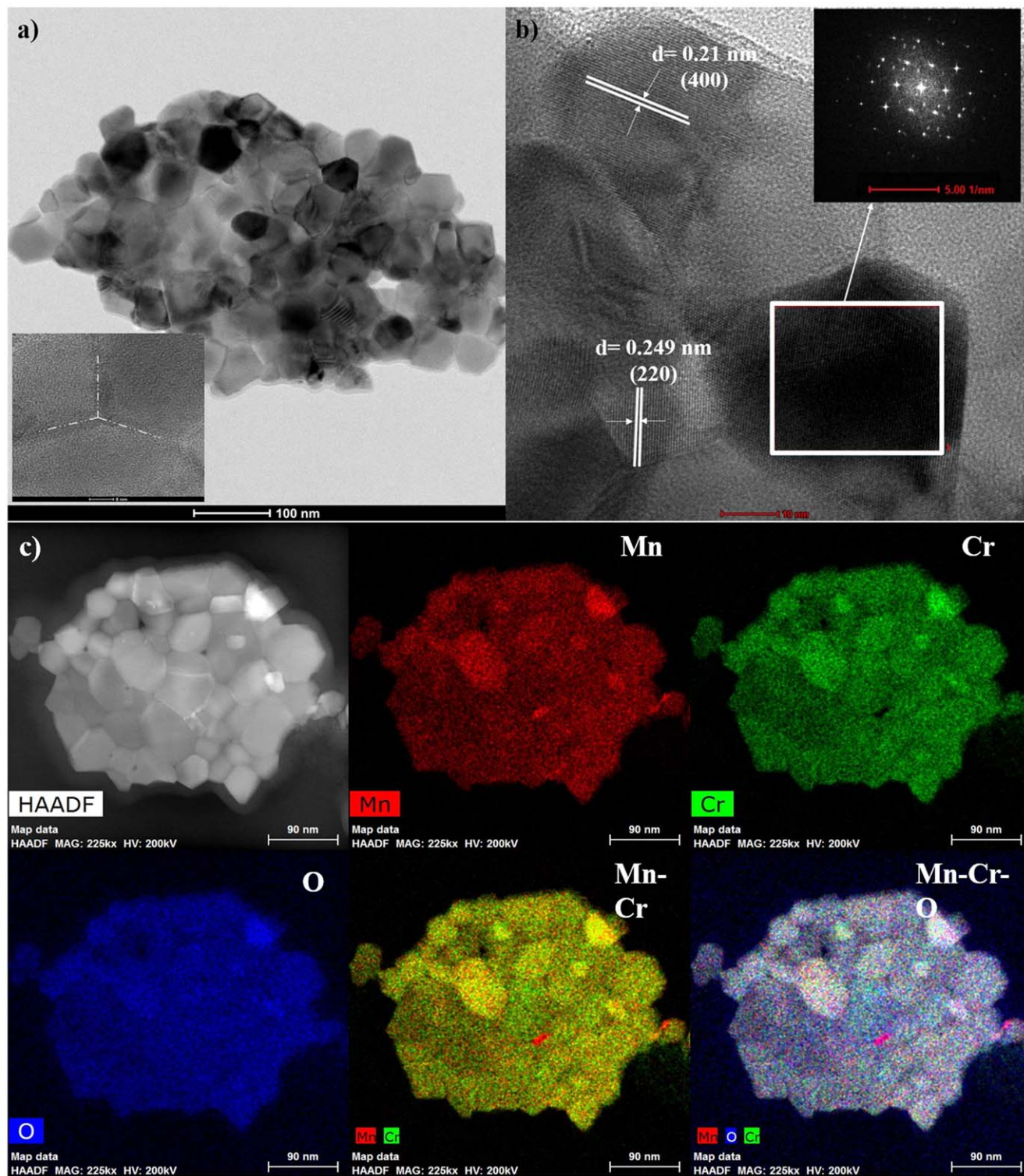


Figure 3. (a) TEM (b) HRTEM and the associated FFT patterns (inset) of the lattice fringes (c) Elemental mapping by high-angle annular dark-field scanning transmission electron microscopy (HAADF-STEM) of Mn, Cr, O and its overlapping in MnCr_2O_4 nanoparticles. Inset Fig. 3a. HRTEM of MnCr_2O_4 with clear particle boundaries.

and 653.4 eV that correspond to Mn $2\text{P}_{3/2}$ and Mn $2\text{p}_{1/2}$ respectively.^{52–54} The deconvolution of each Mn 2p shows the existence of three characteristic peaks at 640.3 eV, 641.9 eV and 644.3 eV assigned to +2, +3 and +4 oxidation states of Mn.^{34,55}

The Co 2p XPS spectrum in Fig. 4b shows the presence of two main peaks at 779.5 eV (Co $2\text{p}_{3/2}$) and 794.6 eV (Co $2\text{p}_{1/2}$) with a splitting of ~ 15 eV. The peaks fitted at 779.7 eV and 794.7 eV are

attributed to +3 oxidation state and the peaks pointed at 780.7 eV and 796.4 eV confirm the presence of +2 state of Co along with some satellite peaks. Similarly, the Cr 2p (Fig. 4e) in MnCr_2O_4 also shows the existence of mixed valence of Cr in +2, +3 and +4 form. The O 1s emission spectrum of MnCo_2O_4 (Fig. c) and MnCr_2O_4 (Fig. f) can be deconvoluted as three distinct peaks at 530.1 eV (O_L), 532.1 eV (O_V) and 533.4 eV (O_V). The peak O_L corresponds to metal

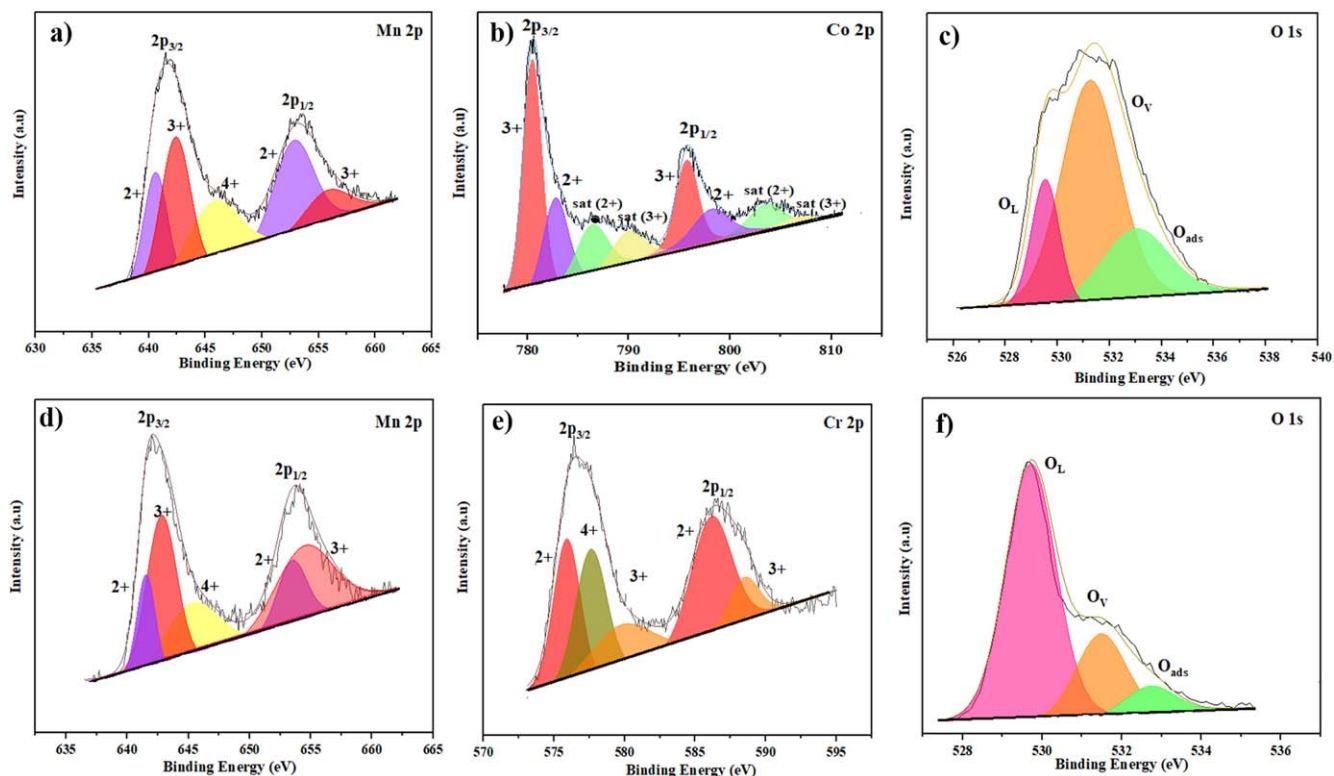


Figure 4. High resolution XPS spectrum of (a) Mn 2p (b) Co 2p (c) O 1s for MnCo_2O_4 and (d) Mn 2p (e) Cr 2p (f) O 1s for MnCr_2O_4 synthesized using solution combustion synthesis.

oxygen bonding sample (M-O) in the prepared sample. O_V ascribe the existence of defect sites with minimum oxygen coordination and O_{ads} is assigned to the physically and chemically adsorbed water molecule on the surface of the catalyst. MnCo_2O_4 exhibits highest ratio of O_V / O_L (2.94) when compared to MnCr_2O_4 (0.81). The higher concentration of oxygen defects in MnCo_2O_4 generate higher density of extra oxygen vacancies, which may favour for a faster reaction rate of oxygen electrode reactions. The presence of abundant oxygen vacancies provide enough catalytically active sites for electrochemical reactions.^{56,57} Surface composition analysis using XPS indicates Co/Mn and Cr/Mn ratio to 2.15 and 0.65 respectively, much different than the bulk value of 2 for both the samples. Surface rearrangement in multimetallic compounds is expected as reported by other authors.^{58,59} As the surface

environment is different compared to bulk, which is also affected by the presence of gaseous phase, elemental redistribution takes place to obtain the most stable arrangement.^{58,59}

Previous reports indicate that the presence of metal ions in higher oxidation states provide a fast and improved charge transport to the reactant molecules and intermediates at electrode-electrolyte interface during an electrochemical reaction.^{45,60,61} De Koninck and co-workers reported a stronger adsorption of electronegative O_2 molecule on Co^{3+} octahedral ions than on the Co^{2+} ions. The Co^{3+} ions are expected to be formed on the surface through a partial substitution of Co^{2+} ions with doped metal ions (M^{2+}), nonetheless, the Co^{3+} -O bond is stronger than Co^{2+} -O bond.^{61,62} In addition, the ratio of $\text{Mn}^{4+}/\text{Mn}^{3+}$ is higher for MnCo_2O_4 (0.833) when compared to MnCr_2O_4 (0.656). The transformation of Mn^{3+} into Mn^{4+} in

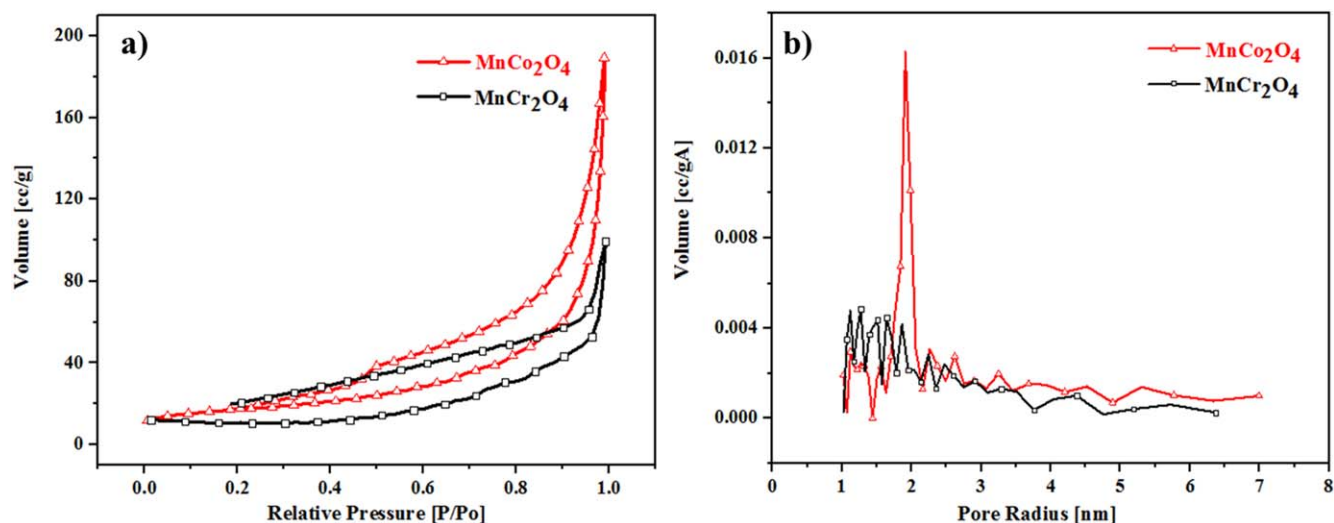


Figure 5. (a) BET surface area and (b) pore size distribution profile of MnCo_2O_4 and MnCr_2O_4 catalysts.

Table I. BET surface area, pore volume, pore size and crystallite size of prepared nanoparticles.

Catalysts	BET area (m ² /g)	Pore Volume (cc/g)	Pore size (nm)	Crystallite size (nm)
MnCo ₂ O ₄	66.769	0.2944	8	13
MnCr ₂ O ₄	28.427	0.15	10.8	18

MnCo₂O₄ is due to a further oxidation of manganese oxide that loses oxygen and cause oxygen vacancy on the surface.⁶³ Significantly, the increased ratio of O_v/O_L and Mn⁴⁺/Mn³⁺ is chemically correlated, and this relation facilitate the oxygen adsorption by providing additional active sites for the ORR/OER electrochemical reaction.

Figure 5 shows the BET surface area and pore size analysis of the as prepared nanomaterials. The BET surface area of MnCo₂O₄ was found to be 66.769 m² g⁻¹, which is ~2.5 times higher than MnCr₂O₄ (28.427 m² g⁻¹). Furthermore, Fig. 5b shows that the synthesized sample consist of small mesopores (2–50 nm) and the pore volume is higher for MnCo₂O₄. The cumulative pore volume of MnCo₂O₄ was measured to be 0.2944 cc/g and for MnCr₂O₄ it holds a value of 0.15 cc/g. The pore size also exhibit same trend as that of

pore volume. The higher pore volume and a larger surface area facilitate the easier adsorption and desorption of gases and the product intermediates, thereby increase in the electrochemical performance. Table I shows the different material properties of the as-synthesized catalysts including BET area, pore volume, pore size and crystallite size.

The electrochemical properties of MnCr₂O₄ and MnCo₂O₄ as an oxygen electrocatalyst were analysed using cyclic voltammetry (CV) and linear sweep voltammetry (LSV) in O₂ saturated 1 M KOH solution as shown in Figs. 6a–6b. In Fig. 6a, the dotted line represents the current response of the catalyst in N₂ saturated 1 M KOH electrolyte at a potential ranging from 0.2 to 1.42 V at a scan rate of 50 mVs⁻¹. The CV (N₂) of MnCo₂O₄/C consists of a couple of strong redox peaks, and indicates the capacitive characteristics of

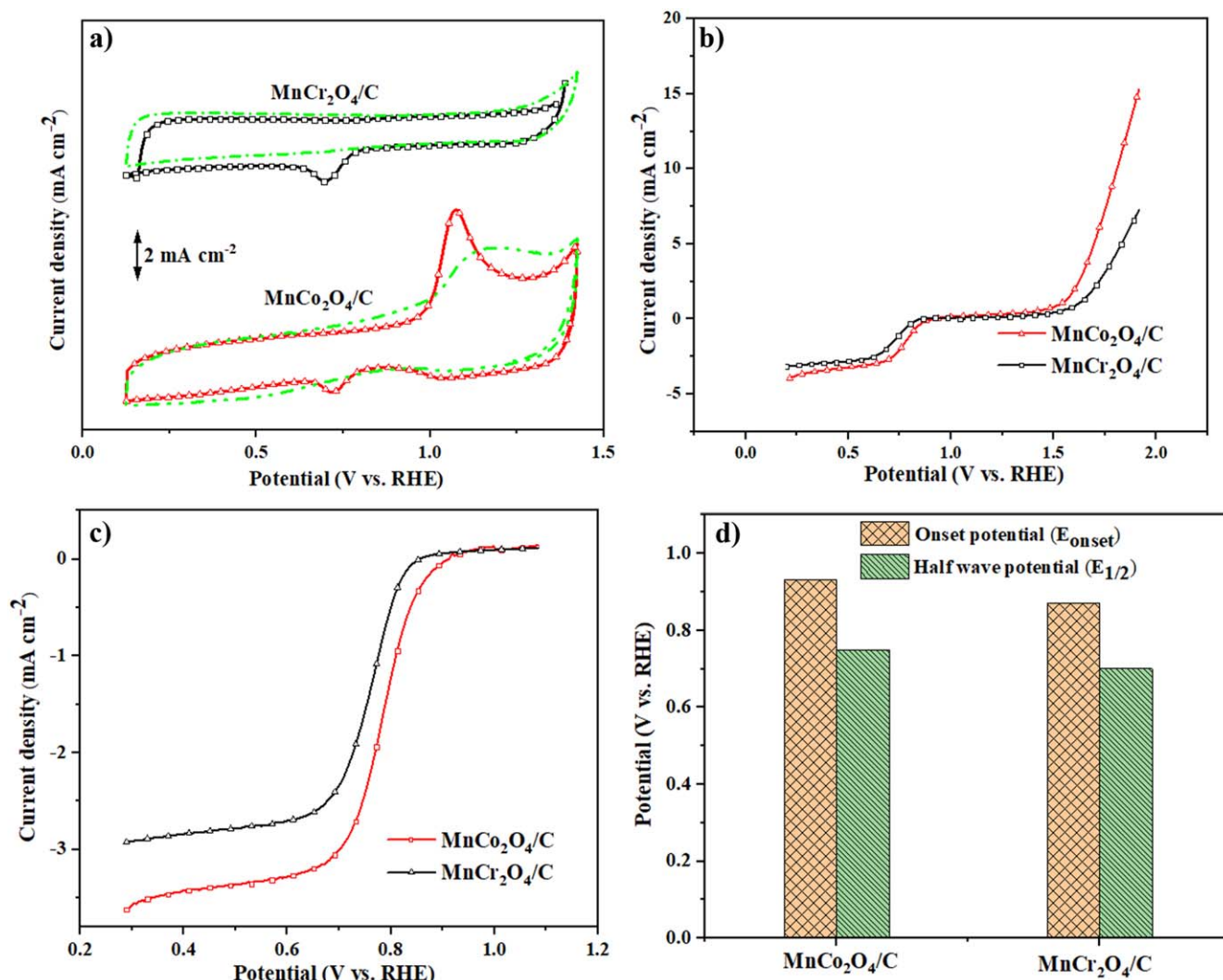


Figure 6. (a) Cyclic voltammogram (CV) in O₂ saturated (solid line) and N₂ saturated (dotted line) 1 M KOH at a scan rate of 50 mVs⁻¹ (b) and Linear Sweep Voltammogram (LSV) at 1600 rpm at 5 mVs⁻¹ of MnCo₂O₄ and MnCr₂O₄ on glassy carbon electrode (c) ORR polarization curve between 0.3 V and 1.1 V (d) The bar plot corresponds to half wave potential and onset potential of the electrocatalysts.

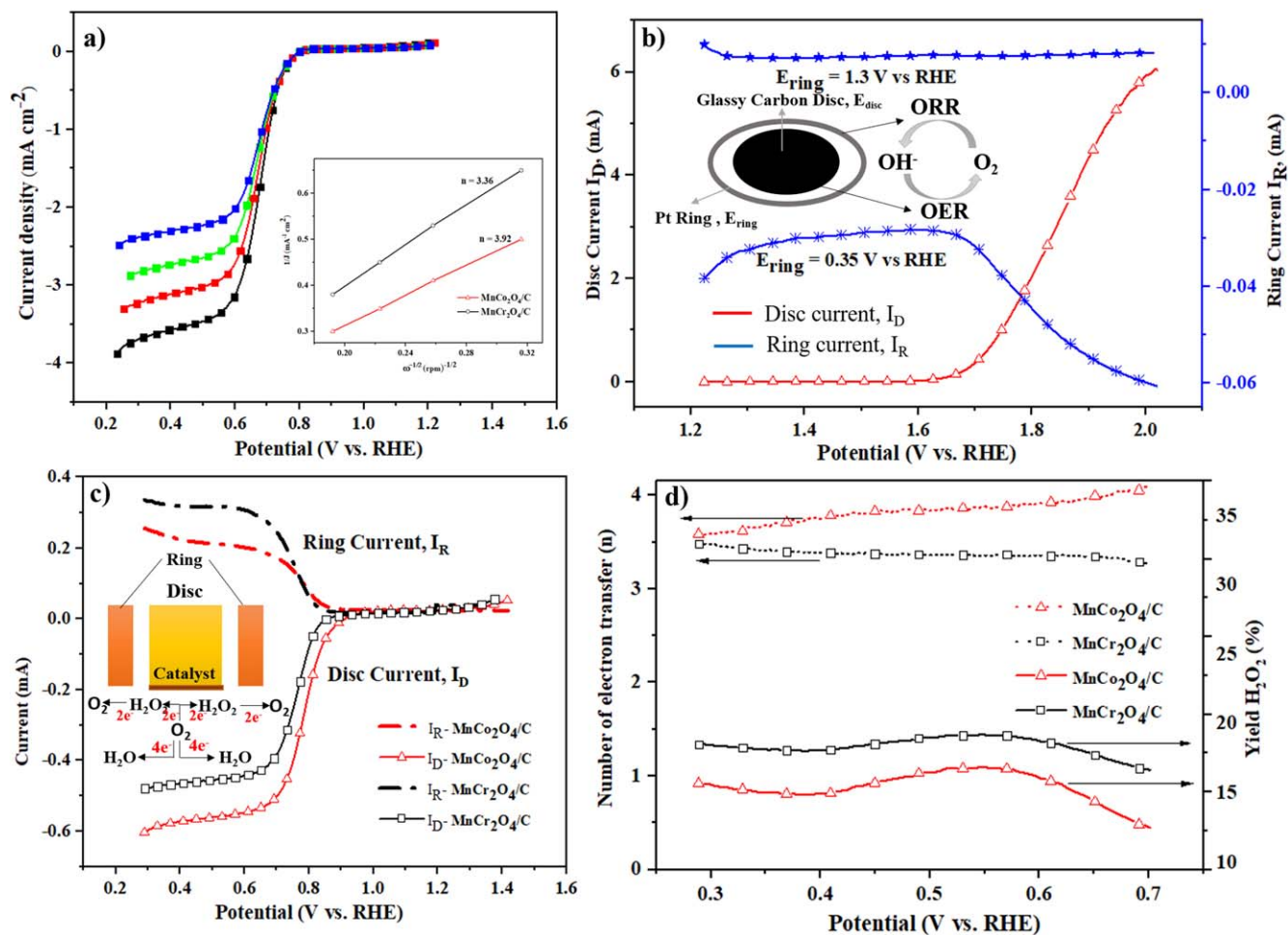
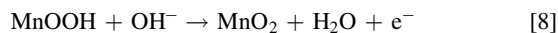


Figure 7. (a) LSV of MnCo_2O_4 at different rotator speed (1600 rpm to 400 rpm). Inset. K-L plot of MnCo_2O_4 for ORR current densities at different rotation and the overall electron transfer in the reaction (b) RRDE detection of O_2 evolution on MnCo_2O_4 with ring potential $E_{\text{ring}} = 1.3$ and 0.35 V in N_2 saturated 1 M KOH solution at 1600 rpm with a scan rate 5 mVs^{-1} (c) RRDE polarization curve with (a) Ring current, I_R (b) Disk current, I_D in O_2 saturated 1 M KOH electrolyte at rotation rate of 1600 rpm (d) calculated number of electron transfer and peroxide yield from RRDE measurements.

faradaic redox reaction. The possible mechanism for this pseudo capacitance and the reversible chemical transformation can be ascribed as:



In case of MnCr_2O_4 there is no such redox couple peaks are visible. The well-defined cathodic peak in O_2 saturated medium corresponds to oxygen reduction reaction (ORR). LSV measurement in Fig. 6b shows the negative reduction current (cathodic current) and positive evolution current (anodic current) corresponds to oxygen reduction reaction (ORR) and oxygen evolution reaction (OER) respectively. This result shows that the selected catalysts are good candidates for fuel cells and battery applications. The main parameters that govern the performance of electrocatalysts are; limiting current density, half wave potential, onset potential and kinetic current density. The ORR LSV curve shown in Fig. 6c indicates that the onset potential (and half wave potential) of ORR are 0.93 V (0.76 V) and 0.87 V (0.7 V) for MnCo_2O_4 and MnCr_2O_4 respectively. It is worth noting that, the kinetic current density calculated at 0.7 V for MnCo_2O_4 (8.6 mAcm^{-1}) is almost 1.7 times higher than MnCr_2O_4 (5.05 mAcm^{-1}). Likewise, MnCo_2O_4 affords higher limiting current density than MnCr_2O_4 that could be due to the mixed oxide fluffy morphology and the presence of more oxygen vacancies that facilitate a smooth passage of electron into and out of the active reaction sites.

The supported carbon helps in further dispersion that prevent the particle agglomeration, thereby enhances the accessible active sites. Besides ORR, the tested catalyst shows excellent activity towards OER. The onset potential of OER in MnCo_2O_4 is lower than MnCr_2O_4 with a current density of 7.6 mAcm^{-1} (MnCo_2O_4) and 3.5 mAcm^{-1} (MnCr_2O_4) at 1.75 V in 1600 rpm. The bifunctional nature of the catalyst is determined by a difference in the onset potential of ORR and OER ($\Delta E = E_{\text{OER}} - E_{\text{ORR}}$), where a smaller difference indicates better bifunctionality. The MnCo_2O_4 catalyst shows a value of ΔE to be 0.59 V, much smaller than MnCr_2O_4 (0.68 V) indicating an improved bifunctional nature of MnCo_2O_4 .

RDE polarization curves at different rotating speed from 400 rpm to 1600 rpm presented in Fig. 7a shows an increase in the limiting current density with an increase in the rotator speed. This is due to a rapid oxygen transport between the electrolyte-catalyst interfaces with shortened diffusion distance at higher speed. The overall number of electron transfer during the oxygen reduction reaction can be obtained using the KL plot at 0.7 V (inset Fig. 7a) based on Eq. 2. The linearity of the KL plot indicates the first order kinetics towards the reduction of dissolved oxygen. The number of electron transfer for MnCo_2O_4 is calculated to be 3.92 and that of MnCr_2O_4 is 3.36 , suggesting that these mixed oxides favor a desirable four-electron oxygen reduction pathway. The higher current densities in the positive potential scan could be from the four-electron transfer reaction during oxygen evolution reaction or from the unfavourable formation of hydrogen peroxide with two electron pathway or else

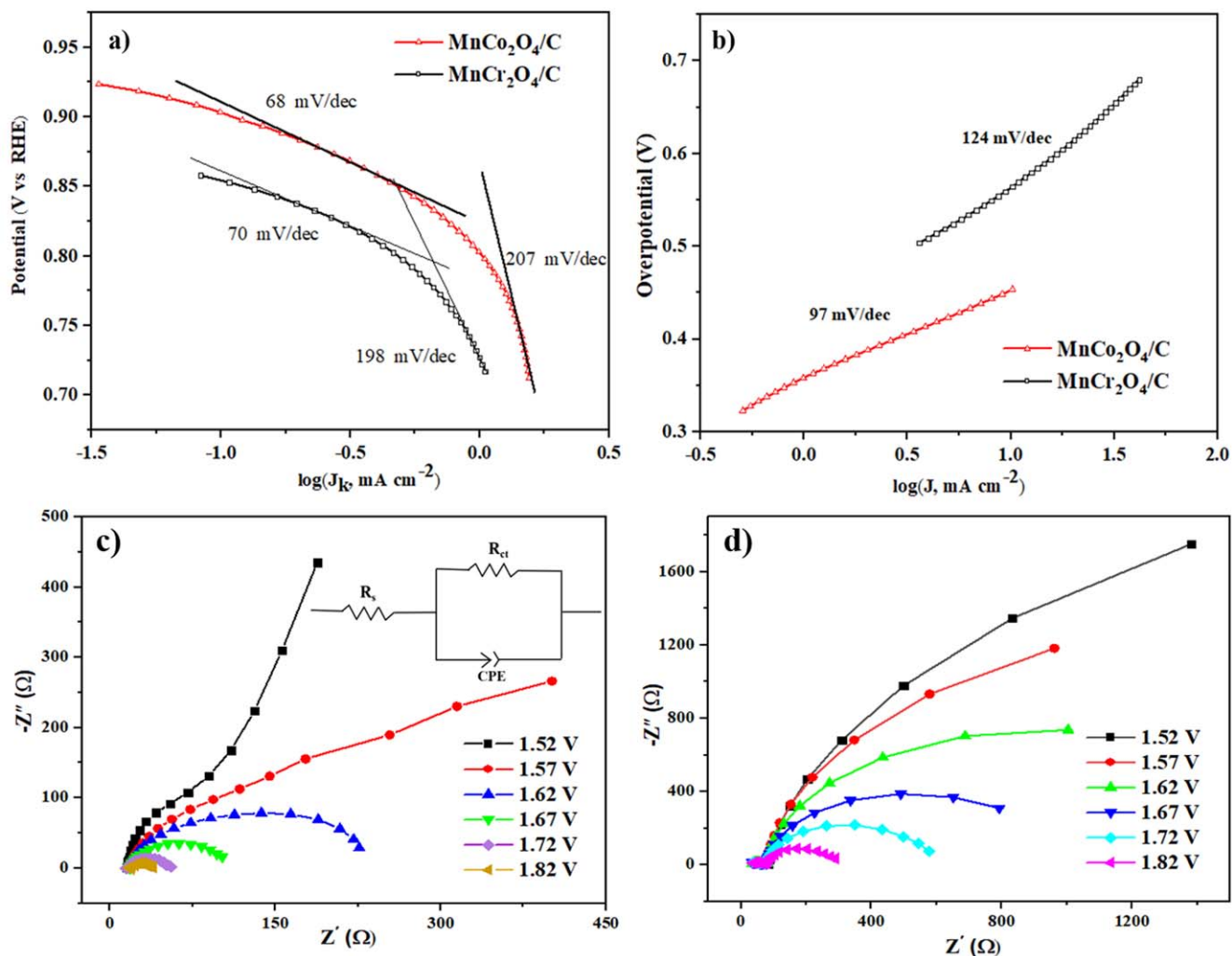


Figure 8. Tafel plot for (a) ORR and (b) OER measured from LSV that shows the activity comparison of MnCo_2O_4 and MnCr_2O_4 in 1 M KOH saturated with O_2 with a rotor speed of 1600 rpm and scan rate 5 mV s^{-1} and EIS Nyquist plot of (c) MnCo_2O_4 and (d) MnCr_2O_4 at different DC potential in 1 M KOH electrolyte. Inset shows the equivalent simple Randle circuit model.

the oxidation of catalyst surface itself can cause some increase in the current value with the applied potential. Rotating ring disc electrode (RRDE) study is conducted to confirm the oxygen evolution reaction with N_2 saturated 1 M KOH. The platinum ring is polarized at a potential where the ORR is mass-transfer controlled at Pt (where the

limiting current is measured) while the potential of the disk (with the catalysts deposited on it) is positively scanned toward a region where the OER takes place in an oxygen-free solution. When $E_{\text{ring}} = 0.35 \text{ V}$, the oxygen evolved in the disc electrode subsequently reduced at Pt ring that is confirmed through the increase in the current values of disc (I_D) and ring (I_R) just above the OER onset potential value. At positive potential of ring, the formation of H_2O_2 could be identified. However, in Fig. 7b when the ring potential ($E_{\text{ring}} = 1.3 \text{ V}$) there is no indication of current rise corresponding to the H_2O_2 . This result confirms that the MnCo_2O_4 follows a four-electron oxygen evolution reaction to produce dioxygen.

The ORR pathway can be identified using the rotating ring disc electrode (RRDE) measurement in O_2 saturated 1 M KOH electrolyte by calculating the number of electron transfer and H_2O_2^- yield. In Fig. 7c, MnCo_2O_4 shows highest disc current and least ring current when compared to MnCr_2O_4 . Such behavior suggests that MnCo_2O_4 possesses effective ORR activity with minimum amount of peroxide formation. The number of electron transfer and H_2O_2^- yield of both catalysts calculated using Eqs. 5 and 6 is shown in Fig. 7d. The number of electron transfer for MnCo_2O_4 and MnCr_2O_4 is found to be in the range of 3.8–4 and 3.2–3.3 respectively, which are consistent with the finding from KL plot. Significantly, the peroxide yield in MnCo_2O_4 (~14%–16%) indicates that the ORR favors four electron transfer through the direct transfer of oxygen to

Table II. Fitted value of the equivalent circuit parameter at different DC potentials for MnCo_2O_4 and MnCr_2O_4 .

Catalysts	Potential	$R_s(\Omega)$	$R_{ct}(\Omega)$	C F $s^{(n-1)}$	n
MnCo_2O_4	1.52	7.2	225	222E^{-6}	0.835
	1.57	7.4	196	197E^{-6}	0.83
	1.62	7.2	70	195E^{-6}	0.87
	1.67	7.8	63.6	185E^{-6}	0.861
	1.72	13.96	31.14	155E^{-6}	0.84
	1.82	9.05	11.41	99.3E^{-6}	0.83
MnCr_2O_4	1.52	74.38	887	261E^{-6}	0.898
	1.57	68.63	772	265E^{-6}	0.891
	1.62	66.48	668	239E^{-6}	0.904
	1.67	65.4	507	228E^{-6}	0.887
	1.72	64.47	263	200E^{-6}	0.871
	1.82	59.49	196	55.5E^{-6}	0.88

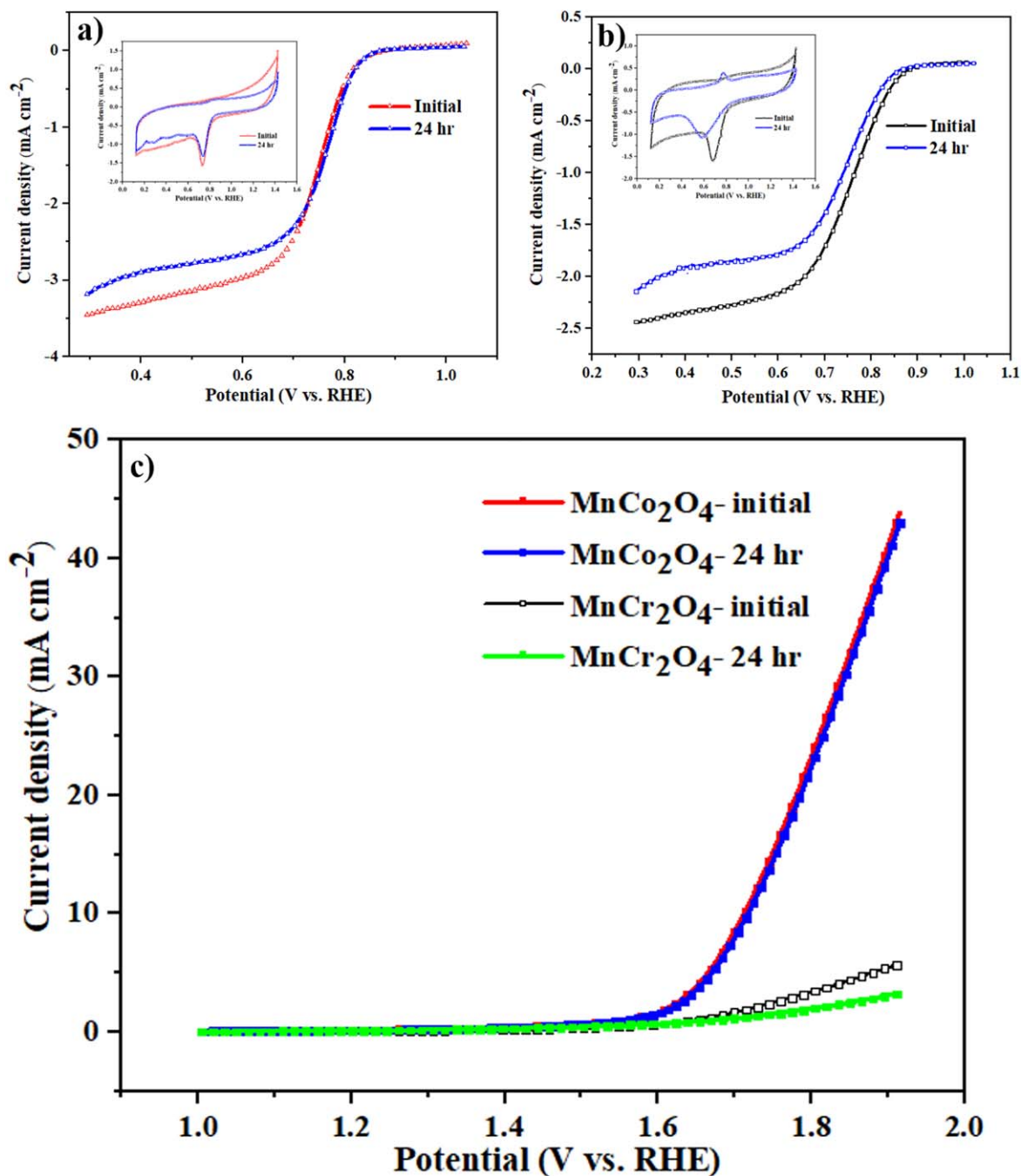


Figure 9. (a) and (b) ORR LSV after stability analysis of MnCo₂O₄ and MnCr₂O₄ in 1 M KOH electrolyte at +0.5 V vs RHE for 24 h. Inset shows the CV after stability (c) LSV corresponding to OER after stability.

hydroxide ions without processing through any product intermediate. In case of MnCo₂O₄, in presence of large number of active sites, the likelihood of desorption of the formed H₂O₂, and its re-adsorption on another site and reactive transformation to H₂O is much higher. Therefore, the amount of H₂O₂ detection in ring electrode will be lower.

The electro kinetics of the anodic and cathodic reactions for oxygen electrocatalysts can be identified using Tafel plots, by plotting logarithm of kinetic current density ($\log J_k$) calculated from KL Eq. 1 on x-axis and applied potential on y-axis as shown in Fig. 8. The ideal Tafel plot consist of two slopes one at lower potential and another one at higher potential corresponding to Temkin and Langmuir isotherms respectively. The oxygen electrocatalysts with a lower slope value at higher potential and a higher

slope at lower potential exhibit enhanced performance towards ORR. Considering this fact, the MnCo₂O₄ with slope values of 68/207 mVdec⁻¹ shows faster ORR kinetics than that of MnCr₂O₄ with values of 70/198 mVdec⁻¹ as indicated in Fig. 8a. The Tafel plot for OER in Fig. 8b shows a value of 97 mVdec⁻¹ and 124 mVdec⁻¹ corresponding to MnCo₂O₄ and MnCr₂O₄, indicating an improved OER response of the former catalyst. The electrochemical process and the electrode kinetics of MnCo₂O₄ and MnCr₂O₄ was further analyzed using EIS method in order to evaluate the various resistances associated with the charge transfer process during OER. The Nyquist plot was drawn with different DC potentials (obtained from OER LSV curve) with an AC perturbation of 10 mV as shown in Figs. 8c–8d. The complete semicircular loop shows that there is no mass transport limitation in the measured potential.⁶⁴

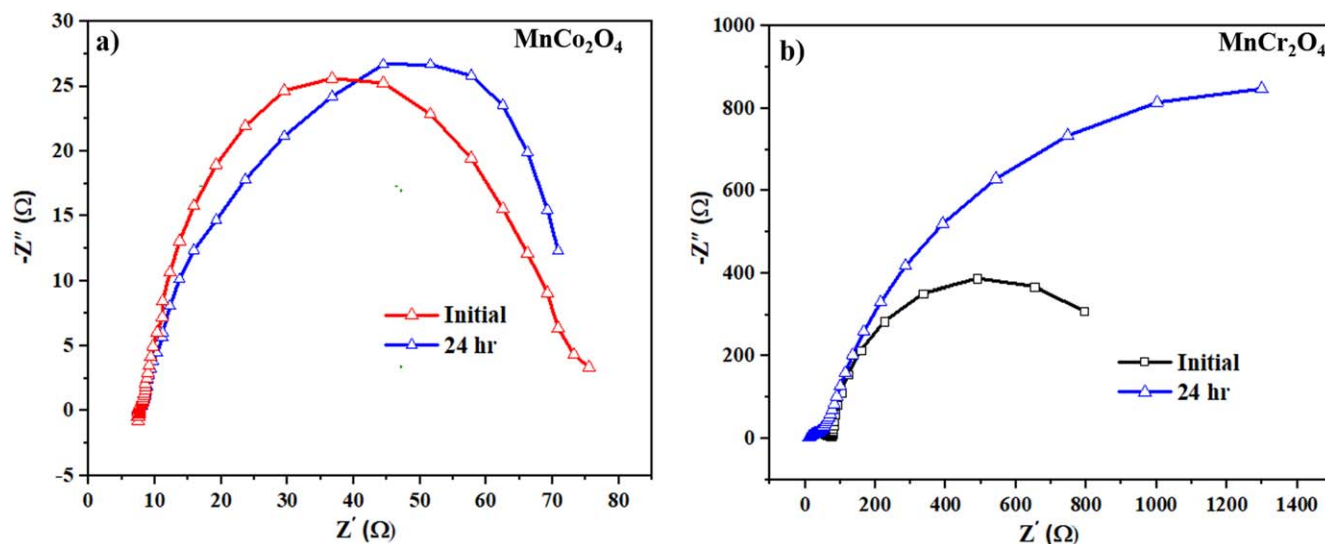


Figure 10. EIS spectrum of (a) MnCo_2O_4 and (b) MnCr_2O_4 before and after 24 h stability run at 1.675 V.

When the applied DC potential increases, the diameter of semicircle decreases indicating a decrease in the barrier of the interfacial OER mechanism.

The Nyquist plot obtained using EIS measurement can be fitted using simple Randle circuit model (inset Fig. 8c) consist of three components with a series resistance (R_s), charge transfer resistance (R_{ct}) and constant phase element (CPE). The series resistance (R_s) was identified from the intercept of the plot with the horizontal axis at high frequency that corresponds to the overall series resistance including the material bulk resistance and contact resistances. The R_{ct} corresponds to the charge transfer resistance across the electrode-solution interface that was calculated from the diameter of the semicircle in Nyquist plot at high frequency region. The double layer capacitive effect in the OER reaction was replaced with the constant phase element (CPE) in order to model depressed semi-circles related to the heterogeneous and porous catalyst surface.⁶⁵ It provides information of the electrocatalytic properties normal to the surface of the catalyst including the oxide layer conductivity and structural reconstruction.

The CPE can be represented as impedance, in general as:

$$Z_{CPE} = 1/[C_f(i\omega)^n]$$

C_f is a frequency-independent constant with unit a of $F\text{ s}^{(n-1)}\text{cm}^{-2}$, ω be the angular frequency of the alternating current signal, i is the imaginary part holding the value of square-root of -1 , n is a variable factor in the range of 0 to 1. If $n = 1$ CPE behaves as pure capacitor. The fit value for each equivalent circuit elements are given in Table II. Somehow, the ohmic resistance (R_s) shows a slight increase with increase in applied potential, which could be due to the generation of gas bubbles that resist the passage of OH^- ions for the OER process.

Indeed, MnCo_2O_4 possess a much smaller R_{ct} when compared with MnCr_2O_4 , suggesting that the former one facilitates faster charge transfer between the catalyst and electrode. If the resistance is low, more OH^- ion absorption will cause increase in the intermediate formation at the interface of electrode and electrolyte that lowers the activation energy of electrochemical reaction.⁶⁶ The Nyquist plot for MnCo_2O_4 and MnCr_2O_4 at 1.657 V, shown in Fig. 8, shows higher impedance value for MnCr_2O_4 due to a higher charge transfer resistance for the electron transportation process of the OER redox. This indicates that MnCo_2O_4 provide large number of active sites on the catalyst surface to facilitate transport of charge carriers between the catalyst and the electrode.

Alkaline tolerance and degradation of the active sites of the catalyst surface are among the main issues facing in the field of oxygen electrocatalysis. The adsorption of the intermediate and the slow desorption blocks the active surface sites for further reaction, reducing their activity. The stability of the oxygen electrocatalyst are identified by monitoring the current density while holding the potential value constant at +0.5 V for 24 h. In order to confirm the activity of the catalyst, CV and LSV measurement were performed for each catalyst as shown in Figs. 9a–9c. The LSV of MnCo_2O_4 shows that there is a slight decrease in the limiting current density, but not much change in the polarization curve in terms of onset potential and half wave potential even after the stability run of 24 h. The oxygen reduction peak in the CV (inset 9a) displays same peak potential and negligible loss in the current density after the stability run. The LSV plot of MnCr_2O_4 in Fig. 9b shows a slight negative shift in the onset potential (0.0082 V) and half-wave potential (0.06 V) after the stability run. Moreover, the CV (Inset Fig. 9b) shows a decrease in the current density along with a shift in the reduction peak towards a negative potential, indicating the instability of the catalyst in long term run.

The stability of OER mechanism is shown in Fig. 9c, it is clear that there is no change in the OER curve corresponding to MnCo_2O_4 , while the current density reduced with respect to time in case of MnCr_2O_4 . The decrease in the activity in MnCr_2O_4 could be due to the change in the physical nature of the catalyst after multiple cycling. On the other hand, the highly porous MnCo_2O_4 structure with high oxygen defect looks to be more stable and the activity is retained even after 24 h.

The EIS Nyquist plot of OER before and after stability test at 1.675 V in Fig. 10 shows that the impedance of MnCo_2O_4 remains same, suggesting the existence of catalytic active sites even after the stability run. There will be a fast adsorption and desorption of the products and/or intermediates that facilitate the higher OER performance. Meanwhile, in MnCr_2O_4 there exist a larger charge transfer resistance that hinders the further catalytic activity of the oxide catalyst. These results are consistent with the LSV measurement in Fig. 9c. From the above study, it is clear that MnCo_2O_4 is a promising bifunctional electrocatalyst in terms of activity and durability for electrochemical applications for ORR and OER. Table III shows a detailed comparison of the performance of MnCo_2O_4 and MnCr_2O_4 catalysts in this work with some previously reported catalysts for ORR/OER applications.

The adsorption of O_2 on the active sites of the catalysts, followed by the O_2 reduction to OH^- is the main rate-determining step in

Table III. Comparison of manganese-based catalysts with recently reported highly active bifunctional oxygen electrocatalyst.

Catalyst	Method	E_{ORR} Onset potential (V vs RHE)	Half wave potential (V vs RHE)	E_{OER} (V vs RHE)	ΔE $E_{\text{OER}} - E_{\text{ORR}}$ (V vs RHE)	Medium	References
MnCo ₂ O ₄ /C	Combustion synthesis	0.93	0.83	1.52	0.59	1 M KOH	This work
MnCr ₂ O ₄ /C	Combustion synthesis	0.87	0.76	1.56	0.68	1 M KOH	This work
MCO/NS-MCS	Hard template method	0.8856	0.8046	1.6356	0.75	0.1 M KOH	33
MnCo ₂ O ₄	Template free method	0.9246	~0.74	—	—	0.1 M KOH	26
dpMnCo ₂ O ₄ /CNT	Hydrothermal	0.8546	~0.714	1.49	0.63	0.1 M KOH	34
dpMnCo ₂ O ₄ /N-rG	Hydrothermal	0.8946	~0.7646	1.55	0.66	0.1 M KOH	34
MnCo ₂ O ₄	Spray-pyrolysis	0.95	~0.82	~1.52	0.57	0.1 M KOH	67
NiCo ₂ O ₄	Self-assembly	0.814	0.6246	1.56	0.746	0.1 M KOH	68
NiCoO ₂ /CNT	One pot method	0.91	0.70	1.40	0.49	0.1 M KOH	69
NiCo ₂ O ₄	Co-precipitation	0.7446	0.6446	0.82	1.56	0.1 M KOH	70
NiCo ₂ O ₄ -rGO Hybrid	Hummer method	0.8846	0.6446	—	—	0.1 M KOH	71

ORR. However, the activity of the catalyst is greatly influenced by the affinity of the catalyst towards oxygen and the available active sites accessible for the reaction. The XPS analysis identifies the existence of a high concentration of oxygen vacant sites in MnCo_2O_4 , which can cause high affinity for O_2 adsorption. Thus adsorbed oxygen molecule directly connect with the metal sites (Mn/Co) leading to the formation of Metal-O bond that in turn elongates the O-O bond and finally reduces the oxygen reduction barrier. The smaller crystallite size, well porous mixed oxide structure, higher oxygen vacancy with more distorted crystal structure, higher surface area and pore volume, high intrinsic catalytic effect, faster electron transfer rate from reactant to product could be the main reason for the outstanding catalytic performance of MnCo_2O_4 .

Conclusion

Single step conventional solution combustion synthesis was used to synthesize highly pure and crystalline nanostructure of MnCo_2O_4 and MnCr_2O_4 . Thus prepared particles were characterized using XRD, SEM, TEM, BET and XPS in order to confirm the phase and morphology. MnCo_2O_4 is in the form of ultra-thin layer of irregular transparent structures that are interweaved to form porous morphology. MnCr_2O_4 particles obtained are in the form of cubic structure with average particle size of 30–50 nm that are interconnected with weak van der Waals interactions with an overlapping of the lattice fringes. Moreover, XPS confirms the existence of MnCo_2O_4 with abundant oxygen vacant sites. The BET analysis shows the presence of highly mesoporous/microporous MnCo_2O_4 with higher surface area and pore volume, which is almost 2 times higher than MnCr_2O_4 . These MnCo_2O_4 exhibit excellent ORR and OER performances in 1 M KOH solution owing to the high oxygen vacancy, large number of exposed catalytic active sites and highly efficient mass transport with minimum charge transfer resistance.

Acknowledgments

This publication was made possible by NPRP grant (NPRP8–145–2–066) from the Qatar National Research Fund (a member of Qatar Foundation). The statements made herein are solely the responsibility of the author(s). The authors also wish to gratefully acknowledge Centre of Advanced Materials (CAM) for XRD analysis and the SEM analysis was accomplished in the Central Laboratories Unit, Qatar University. The authors would also like to acknowledge QEERI Core Labs for their support related to the TEM characterization.

References

1. A. S. Arico, P. Bruce, B. Scrosati, J. Tarascon, and W. Van Schalkwijk, *Nat. Mater.*, **4**, 5 (2005).
2. J. Choi, D. Higgins, and Z. Chen, *J. Electrochem. Soc.*, **159**, 1 (2011).
3. F. Cheng and J. Chen, *Chem. Soc. Rev.*, **41**, 6 (2012).
4. J. Salminen, D. Steingart, and T. Kallio, in *Future Energy* (Elsevier, Amsterdam) p. 259 (2008).
5. Y. Gorlin and T. F. Jaramillo, *J. Am. Chem. Soc.*, **132**, 39 (2010).
6. N. Sasikala, K. Ramya, and K. Dhathathreyan, *Energy Convers. Manage.*, **77**, 545 (2014).
7. K. Fu, Y. Wang, L. Mao, X. Yang, W. Peng, J. Jin, S. Yang, and G. Li, *J. Power Sources*, **421** (2019).
8. S. Jiang, K. Ithisuphalap, X. Zeng, G. Wu, and H. Yang, *J. Power Sources*, **399** (2018).
9. J. Greeley, I. Stephens, A. Bondarenko, T. P. Johansson, H. A. Hansen, T. Jaramillo, J. Rossmeisl, I. Chorkendorff, and J. K. Nørskov, *Nat. Chem.*, **1**, 7 (2009).
10. F. Lima, J. Zhang, M. Shao, K. Sasaki, M. Vukmirovic, E. Ticianelli, and R. Adzic, *J. Phys. Chem. C*, **111**, 1 (2007).
11. N. Subramanian, T. Greszler, J. Zhang, W. Gu, and R. Makharia, *J. Electrochem. Soc.*, **159**, 5 (2012).
12. J. N. Schwämmlein, G. S. Harzer, P. Pfändner, A. Blankenship, H. A. El-Sayed, and H. A. Gasteiger, *J. Electrochem. Soc.*, **165**, 15 (2018).
13. Y. Zhao, M. Luo, S. Chu, M. Peng, B. Liu, Q. Wu, P. Liu, F. M. de Groot, and Y. Tan, *Nano Energy*, **59**, 146 (2019).
14. N. Mamaca, E. Mayousse, S. Arrii-Clacens, T. Napporn, K. Servat, N. Guillet, and K. Kokoh, *Appl. Catal. B*, **111**, 376 (2012).

15. M. Inaba, H. Yamada, J. Tokunaga, and A. Tasaka, *Electrochem. Solid-State Lett.*, **7**, 12 (2004).
16. X. Leng, Y. Shao, L. Wu, S. Wei, Z. Jiang, G. Wang, Q. Jiang, and J. Lian, *J. Mater. Chem. A*, **4**, 26 (2016).
17. E. Rios, S. Abarca, P. Daccarett, H. N. Cong, D. Martel, J. Marco, J. Gancedo, and J. Gautier, *Int. J. Hydrogen Energy*, **33**, 19 (2008).
18. R. Ding, L. Qi, M. Jia, and H. Wang, *Electrochim. Acta*, **107**, 494 (2013).
19. Y. Huang, Y. Miao, H. Lu, and T. Liu, *Chem.—Eur. J.*, **21**, 28 (2015).
20. E. Rios, J. Gautier, G. Poillerat, and P. Chartier, *Electrochim. Acta*, **44**, 8 (1998).
21. I. M. Mosa, S. Biswas, A. M. El-Sawy, V. Botu, C. Guild, W. Song, R. Ramprasad, J. F. Rusling, and S. L. Suib, *J. Mater. Chem. A*, **4**, 2 (2016).
22. Q. Wang, Y. Xue, S. Sun, S. Yan, H. Miao, and Z. Liu, *J. Power Sources*, **435**, 226761 (2019).
23. A. Serov, N. I. Andersen, A. J. Roy, I. Matanovic, K. Artyushkova, and P. Atanassov, *J. Electrochem. Soc.*, **162**, 4 (2015).
24. H. Du, Y. Li, F. Ding, J. Zhao, X. Zhang, Y. Li, R. Zhao, M. Cao, T. Yu, and X. Xu, *Int. J. Hydrogen Energy*, **43**, 32 (2018).
25. J. Wang, Y. Fu, Y. Xu, J. Wu, J. Tian, and R. Yang, *Int. J. Hydrogen Energy*, **41**, 21 (2016).
26. T. Y. Ma, Y. Zheng, S. Dai, M. Jaroniec, and S. Z. Qiao, *J. Mater. Chem. A*, **2**, 23 (2014).
27. S. Ghosh, P. Kar, N. Bhandary, S. Basu, S. Sardar, T. Maiyalagan, D. Majumdar, S. K. Bhattacharya, A. Bhaumik, and P. Lemmens, *Catal. Sci. Technol.*, **6**, 5 (2016).
28. Y. Hang, C. Zhang, X. Luo, Y. Xie, S. Xin, Y. Li, D. Zhang, and J. B. Goodenough, *J. Power Sources*, **392** (2018).
29. S. Kosasang, N. Ma, N. Phatharasupakun, and M. Sawangphruk, *J. Electrochem. Soc.*, **166**, 8 (2019).
30. A. Ashok, A. Kumar, R. R. Bhosale, F. Almomani, S. Mohd Ali H Saleh, S. Suslov, and F. Tarlochan, *Int. J. Hydrogen Energy*, **44**, 1 (2019).
31. Y. Liang, Y. Li, H. Wang, J. Zhou, J. Wang, T. Regier, and H. Dai, *Nat. Mater.*, **10**, 10 (2011).
32. G. Li, K. Zhang, M. A. Mezaal, and L. Lei, *Int. J. Electrochem. Sci.*, **10**, 12 (2015).
33. T. Oh, S. Ryu, H. Oh, and J. Kim, *Dalton Trans.*, **48**, 3 (2019).
34. X. Ge, Y. Liu, F. T. Goh, T. A. Hor, Y. Zong, P. Xiao, Z. Zhang, S. H. Lim, B. Li, and X. Wang, *ACS Appl. Mater. Interfaces*, **6**, 15 (2014).
35. C. Li, X. Han, F. Cheng, Y. Hu, C. Chen, and J. Chen, *Nat. Commun.*, **6**, 7345 (2015).
36. S. T. Aruna and A. S. Mukasyan, *Curr. Opin. Solid State Mater. Sci.*, **12**, 3 (2008).
37. A. Cross, A. Kumar, E. E. Wolf, and A. S. Mukasyan, *Ind. Eng. Chem. Res.*, **51**, 37 (2012).
38. A. Varma, A. S. Mukasyan, K. T. Deshpande, P. Pranda, and P. R. Erri, *MRS Proc.*, **800**, AA4.1 (2003).
39. K. Deshpande, A. Mukasyan, and A. Varma, *Chem. Mater.*, **16**, 24 (2004).
40. K. V. Manukyan, A. Cross, S. Roslyakov, S. Rouvimov, A. S. Rogachev, E. E. Wolf, and A. S. Mukasyan, *J. Phys. Chem. C*, **117**, 46 (2013).
41. A. Kumar, E. Wolf, and A. Mukasyan, *AIChE J.*, **57**, 8 (2011).
42. W. Chen, F. Li, J. Yu, and L. Liu, *Mater. Sci. Engin.: B*, **133**, 1 (2006).
43. K. Boobalan, A. Varun, R. Vijayaraghavan, K. Chidambaram, and U. K. Mudali, *Ceram. Int.*, **40**, 4 (2014).
44. A. Ashok, A. Kumar, J. Ponraj, S. A. Mansour, and F. Tarlochan, *Appl. Catal. B*, **254** (2019).
45. A. Ashok, A. Kumar, J. Ponraj, S. A. Mansour, and F. Tarlochan, *Int. J. Hydrogen Energy*, **44**, 31 (2019).
46. A. Ashok, A. Kumar, M. A. Matin, and F. Tarlochan, *J. Electroanal. Chem.*, **844** (2019).
47. A. Ashok, A. Kumar, R. R. Bhosale, M. A. H. Saleh, and L. J. P. van den Broeke, *RSC Adv.*, **5**, 36 (2015).
48. A. Ashok, A. Kumar, R. R. Bhosale, M. A. H. Saleh, U. K. Ghosh, M. Al-Marri, F. A. Almomani, M. M. Khader, and F. Tarlochan, *Ceram. Int.*, **42**, 11 (2016).
49. A. Ashok, A. Kumar, R. R. Bhosale, F. Almomani, S. S. Malik, S. Suslov, and F. Tarlochan, *J. Electroanal. Chem.*, **809** (2018).
50. S. Ma, L. Sun, L. Cong, X. Gao, C. Yao, X. Guo, L. Tai, P. Mei, Y. Zeng, and H. Xie, *J. Phys. Chem. C*, **117**, 49 (2013).
51. A. Patterson, *Phys. Rev.*, **56**, 10 (1939).
52. D. P. Dubal, D. S. Dhawale, R. R. Salunkhe, and C. D. Lokhande, *J. Electrochem. Soc.*, **157**, 7 (2010).
53. X. Li, M. Xin, S. Guo, T. Cai, D. Du, W. Xing, L. Zhao, W. Guo, Q. Xue, and Z. Yan, *Electrochim. Acta*, **253**, 302 (2017).
54. P. W. Menezes, A. Indra, V. Gutkin, and M. Driess, *Chem. Commun.*, **53**, 57 (2017).
55. S. Nagamuthu, S. Vijayakumar, S. Lee, and K. Ryu, *Appl. Surf. Sci.*, **390**, 202 (2016).
56. S. Peng, X. Han, L. Li, S. Chou, D. Ji, H. Huang, Y. Du, J. Liu, and S. Ramakrishna, *Adv. Energy Mater.*, **8**, 22 (2018).
57. N. Kim, Y. J. Sa, T. S. Yoo, S. R. Choi, R. A. Afzal, T. Choi, Y. Seo, K. Lee, J. Y. Hwang, and W. S. Choi, *Sci. Adv.*, **4**, 6 (2018).
58. F. Tao, M. E. Grass, Y. Zhang, D. R. Butcher, F. Aksoy, S. Aloni, V. Altoc, S. Alayoglu, J. R. Renzas, and C. Tsung, *J. Am. Chem. Soc.*, **132**, 25 (2010).
59. A. Kumar, J. Miller, A. Mukasyan, and E. Wolf, *Appl. Catal., A*, **467**, 593 (2013).
60. J. Shen, X. Li, N. Li, and M. Ye, *Electrochim. Acta*, **141** (2014).
61. S. G. Mohamed, Y. Tsai, C. Chen, Y. Tsai, T. Hung, W. Chang, and R. Liu, *ACS Appl. Mater. Interfaces*, **7**, 22 (2015).
62. M. De Koninck, S. Poirier, and B. Marsan, *J. Electrochem. Soc.*, **153**, 11 (2006).

63. A. Machocki, T. Ioannides, B. Stasinska, W. Gac, G. Avgouropoulos, D. Delimaris, W. Grzegorzcyk, and S. Pasieczna, *J. Catal.*, **227**, 2 (2004).
64. X. R. Yuan, C. Song, H. Wang, and J. Zhang, in *Electrochemical Impedance Spectroscopy in PEM Fuel Cells: Fundamentals and Applications* (Springer Science & Business Media, Vancouver) (2009).
65. M. E. Orazem and B. Tribollet, *Angew. Chem. Int. Ed.*, **48**, 1532 (2009).
66. X. Cui, B. Zhang, C. Zeng, and S. Guo, *MRS Commun.*, **8**, 3 (2018).
67. W. Wang, L. Kuai, W. Cao, M. Huttula, S. Ollikkala, T. Ahopelto, A. Honkanen, S. Huotari, M. Yu, and B. Geng, *Angew. Chem. Int. Ed.*, **56**, 47 (2017).
68. L. Liu, J. Wang, Y. Hou, J. Chen, H. Liu, J. Wang, and Y. Wu, *Small*, **12**, 5 (2016).
69. L. Ma, H. Zhou, Y. Sun, S. Xin, C. Xiao, A. Kumatani, T. Matsue, P. Zhang, S. Ding, and F. Li, *Electrochim. Acta*, **252**, 602 (2017).
70. C. Jin, F. Lu, X. Cao, Z. Yang, and R. Yang, *J. Mater. Chem. A*, **1**, 39 (2013).
71. G. Zhang, B. Y. Xia, X. Wang, and X. W. Lou, *Adv. Mater.*, **26**, 15 (2014).